

Explainable AI for Accelerated Microstructure Imaging: A SHAP-Guided Protocol on the Connectome 2.0 scanner

Quentin Uhl¹, Tommaso Pavan¹, Julianna Gerold¹, Kwok-Shing Chan², Yohan Jun², Shohei Fujita², Aneri Bhatt², Yixin Ma², Qiaochu Wang², Hong-Hsi Lee², Susie Y. Huang², Berkin Bilgic², and Ileana Jelescu¹

Abstract—The diffusion MRI Neurite Exchange Imaging model offers a promising framework for probing gray matter microstructure by estimating parameters such as compartment sizes, diffusivities, and inter-compartmental water exchange time. However, existing protocols require long scan times. This study proposes a reduced acquisition scheme for the Connectome 2.0 scanner that preserves model accuracy while substantially shortening scan duration. We developed a data-driven framework using explainable artificial intelligence with a guided recursive feature elimination strategy to identify an optimal 8-feature subset from a 15-feature protocol. The performance of this optimized protocol was validated in vivo and benchmarked against the full acquisition and alternative reduction strategies. Parameter accuracy, preservation of anatomical contrast, and test-retest reproducibility were assessed. The reduced protocol yielded parameter estimates and cortical maps comparable to the full protocol, with low estimation errors in synthetic data and minimal impact on test-retest variability. Compared to theory-driven and heuristic reduction schemes, the optimized protocol demonstrated superior robustness, reducing the deviation in water exchange time estimates by over two-fold. In conclusion, this hybrid optimization framework enables viable imaging of neurite exchange in 14 minutes without loss of parameter fidelity. This approach supports the broader application of exchange-sensitive diffusion magnetic resonance imaging in neuroscience and clinical research, and offers a generalizable method

for designing efficient acquisition protocols in biophysical parameter mapping.

Index Terms—Diffusion MRI, gray matter, microstructure, protocol optimization, explainable AI (XAI), Neurite Exchange Imaging (NEXI).

I. INTRODUCTION

Mapping cortical microstructure is a priority for detecting early changes in neurodegenerative and neuropsychiatric disorders [1]–[3]. Pathologies are often marked by subtle alterations in gray matter cytoarchitecture that precede volumetric atrophy. Advanced diffusion MRI (dMRI) techniques enable noninvasive quantification of these processes by modeling the mean squared displacement of water molecules in tissue [4], [5].

Biophysical dMRI models have extended the utility of diffusion imaging beyond empirical metrics to estimate biologically relevant parameters such as neurite density, intra- and extra-cellular diffusivities, exchange rates, and soma size [6]–[9].

However, assumptions from models developed for white matter are challenged by the complex cytoarchitecture of cortical gray matter. While several extensions have emerged, the Neurite Exchange Imaging (NEXI) model [10] is particularly appealing as it models the exchange between intra- and extra-neurite spaces to estimate an apparent exchange time, t_{ex} , alongside intra-neurite diffusivity D_i , extra-neurite diffusivity D_e , and the intra-neurite volume fraction f . This approach avoids the increased complexity and potential fitting instability of models that also incorporate spherical soma compartments, such as SANDI [11]. The focus on exchange is further justified by evidence that it dominates the signal evolution at typical diffusion times [10], [12], [13].

Recent studies on 3 Tesla Connectome 1.0 and clinical-grade scanners have shown that NEXI can be implemented in humans, and that the estimated exchange time correlates strongly with myelin-sensitive imaging metrics such as the myelin water fraction (MWF) [14], [15]. These findings establish t_{ex} as a potential biomarker of membrane permeability and myelination, with spatial maps revealing biologically plausible patterns across the cortex. However, the underlying acquisition protocols are lengthy (typically >30 minutes) as they require extensive sampling across both gradient amplitude and diffusion time

This work was supported in part by the Swiss National Science Foundation (SNSF) under Eccellenza grant PCEFP2.194260 and an SNSF Mobility Grant; by the National Institutes of Health (NIH) under grants R01 EB028797, R01 EB032378, R01 EB034757, R21 AG082377, R21 EB036105, P41 EB030006, U01 EB026996, and UG3 EB034875; and by NWO/ZonMw under Rubicon award 04520232330012. (Corresponding author: Quentin Uhl, e-mail: quentin.uhl@chuv.ch.)

Q. Uhl, T. Pavan, and I. Jelescu are with the Department of Radiology, Lausanne University Hospital (CHUV) and University of Lausanne, Lausanne, 1011, Switzerland (e-mail: quentin.uhl@chuv.ch; tommaso.pavan@chuv.ch; ileana.jelescu@chuv.ch).

Q. Wang is with the École Polytechnique Fédérale de Lausanne (EPFL), Lausanne, 1015, Switzerland (e-mail: qiaochu.wang@epfl.ch).

J. Gerold, K.-S. Chan, Y. Jun, S. Fujita, A. Bhatt, Y. Ma, H.-H. Lee, S. Y. Huang, and B. Bilgic are with the Department of Radiology, Massachusetts General Hospital, Athinoula A. Martinos Center for Biomedical Imaging, Boston, MA, 02129, USA (e-mail: JGEROLD1@mgh.harvard.edu; kchan2@mgh.harvard.edu; YJUN@mgh.harvard.edu; sfujita@mgh.harvard.edu; abhatt7@mgh.harvard.edu; YMA12@mgh.harvard.edu; HLEE84@mgh.harvard.edu; Susie.Huang@mgh.harvard.edu; BBILGIC@mgh.harvard.edu).

B. Bilgic and I. Jelescu share joint last authorship.

dimensions (i.e. the acquisition of multi-b, multi-t data). The long acquisition time limits the scalability of NEXI in clinical and research settings where scan time, subject motion and compliance are critical constraints [3], [16].

The introduction of the Connectome 2.0 scanner [17], [18] offers new opportunities for advanced dMRI protocol design. With 500 mT/m gradients and 600 T/m/s slew rates, it enables high b-values and short diffusion times (achieved with short gradient pulse separations, Δ), essential for probing fast exchange and structural disorder [19]. Furthermore, the enhanced hardware performance provides a unique ground truth for validating estimations from clinical scanners with lower gradient strengths. On this platform, the standard NEXI model becomes more viable, as gradient pulse durations ($\delta = 5$ ms) approach the idealized NPA, reducing the need for pulse-width corrections [19]. Yet, even on Connectome 2.0, total acquisition time remains a bottleneck. Reducing the number of (b , Δ) combinations while preserving parameter accuracy is therefore essential for clinical translation.

Protocol optimization has traditionally relied on analytic tools like the Fisher Information Matrix (FIM) [20], [21], which quantify theoretical identifiability. However, FIM relies on ideal assumptions, such as Gaussian noise and an unbiased estimator, and cannot fully account for practical challenges like model degeneracy, which often leads to fitting instability.

In this context, data-driven strategies based on machine learning offer a powerful complement to theory-driven approaches. To address the challenge of model opacity, which can hinder clinical trust, we leverage explainable artificial intelligence (XAI). We adopt a framework combining three key components: gradient-boosted decision trees (XGBoost), SHapley Additive exPlanations (SHAP), and Recursive Feature Elimination (RFE) [22], [23]. In this pipeline, XGBoost learns the complex relationships within the data, while SHAP assigns a theoretically grounded importance value to each acquisition condition, the explanation. RFE then progressively prunes the least informative features based on these SHAP rankings. Together, this XGBoost-SHAP-RFE pipeline provides an explainable and scalable approach to acquisition design, with successful applications in medical imaging [24], [25], neuroscience [26], and other scientific domains such as environmental monitoring, cybersecurity, and user modeling [27]–[29].

In this study, we extend this approach to diffusion MRI. We train XGBoost models on synthetic NEXI signals and use SHAP-based RFE to identify the smallest protocol subset that preserves estimation accuracy for t_{ex} , f , D_i , and D_e . We then benchmark this XAI-optimized protocol against FIM-optimized and naive baselines, validate it in vivo on Connectome 2.0, and assess its fidelity, reproducibility, and adaptability to higher-resolution imaging. This work highlights the promise of interpretable machine learning for advancing diffusion model design and making advanced microstructural imaging more accessible in both research and clinical contexts.

II. METHODS

A. Participants

Seven healthy adult volunteers (3 males, mean age 30.3 ± 4.0 years) were scanned under informed consent in accordance

with institutional ethical guidelines. Each participant underwent two identical scan sessions on the Connectome 2.0 MRI system, performed one after the other, to evaluate test-retest reproducibility of NEXI parameter estimation.

B. MRI acquisition

All imaging was performed on a MAGNETOM Connectom.X 3T scanner (Siemens Healthineers) equipped with a 500 mT/m gradient amplitude and 600 T/m/s slew rate [18], using a 72-channel head coil [30]. Diffusion-weighted imaging (DWI) was acquired with a single-shot spin-echo EPI sequence and monopolar gradient pulses. Imaging parameters were: voxel size = 2 mm isotropic, TR/TE = 3300/66 ms, matrix size = 96×96 , 72 axial slices, partial Fourier = 6/8, in-plane acceleration = 2 and simultaneous multislice (SMS) acceleration = 2.

The full protocol was a comprehensive acquisition scheme designed heuristically to ensure broad sampling of the acquisition parameter space. It consisted of 15 (b , Δ) combinations, spanning b-values from 1.0 to 12.5 ms/ μm^2 and diffusion gradient separations Δ from 12 to 45 ms, with a fixed gradient duration $\delta = 5$ ms (where the effective diffusion time is defined as $t_d = \Delta - \delta/3$). Directional sampling ranged from 20 to 64 directions depending on b-value (20 directions at $b = 1000$, 30 at $b = 2500$, 32 at $b = 5000$, 34 at $b = 7350 - 7500$, 44 at $b = 10000$, and 64 at $b = 12500$ ms/ μm^2). Non-diffusion-weighted images ($b = 0$) were acquired at five Δ values, totaling 13 volumes. Total scan time was approximately 27 minutes.

The reduced protocol retained 8 features selected via a SHAP-based feature elimination strategy (see below), with 250 directions in total and identical $b = 0$ sampling. Acquisition time for the reduced protocol was 14 minutes. The 8 selected features spanned a broad range of b-values and diffusion times: (b, Δ) pairs of (1.0, 12), (2.5, 12), (5.0, 15), (7.3, 20), (1.0, 27), (1.0, 45), (2.5, 45) and (12.5, 45) ms/ μm^2 and ms, respectively. Both protocols were pre-processed and processed independently to allow for a matched comparison.

To enable cortical segmentation, a high-resolution T1-weighted anatomical scan (MPRAGE) was collected during each session with 0.9 mm isotropic resolution (TR/TE = 2500/2.9 ms, TI = 1100 ms, flip angle = 8°).

C. Preprocessing

For each protocol, all diffusion-weighted volumes were jointly preprocessed using a standardized pipeline. This process began with complex-domain Marchenko-Pastur Principal Component Analysis (MP-PCA) denoising [31]. To correct for slowly varying phase variations, a two-pass procedure was employed: an initial MP-PCA pass was run on the complex data, the low-pass filtered phase from this output was used to correct the original data's phase, and a final MP-PCA pass was applied to the phase-corrected data. The real part of this final result was used for subsequent steps. The pipeline then continued with Gibbs ringing correction [32], susceptibility-induced distortion and eddy current correction via FSL's `topup` and `eddy` tools [33], and finally, gradient nonlinearity correction using scanner-specific maps [17].

T_1 -weighted images were segmented using FastSurfer [34], and gray matter regions of interest (ROIs) from the Desikan-Killiany-Tourville (DKT) atlas [35] were projected from T_1 to diffusion space via affine registration with ANTs [36].

D. Model fitting

For each protocol, powder-averaged diffusion signals were calculated and NEXI was fitted using nonlinear least-squares optimization [10]. Estimated parameters included intra-neurite diffusivity (D_i), extra-neurite diffusivity (D_e), intra-neurite signal fraction (f), and inter-compartment exchange time (t_{ex}). Fitting bounds and initialization were consistent with previous implementations on 3T Prisma and Connectome 1.0 MRI systems [14], [15]. Cortical surfaces and parameter maps were visualized using Connectome Workbench [37].

E. Synthetic simulations and protocol reduction

A synthetic dataset of 10^6 diffusion signals was generated with the NEXI model. Ground-truth parameter vectors were sampled uniformly within empirical bounds obtained from the full 15-feature protocol (t_{ex} : [1, 70] ms, f : [0.15, 0.80], D_i : [1.7, 3.5] $\mu\text{m}^2/\text{ms}$, D_e : [0.5, 1.5] $\mu\text{m}^2/\text{ms}$). These empirically derived ranges ensured that the simulations covered only physiologically plausible values while avoiding extreme outliers observed in low SNR voxels. Gaussian noise was then added so that the resulting SNR matched the in vivo distribution (mean: 32, CI: [13, 60]). The four NEXI target parameters were z-scored before training, meaning we subtracted the mean and divided by the standard deviation for each parameter. This step ensures all parameters are on a common scale, which is essential for providing fair, unitless feature attributions.

An XGBoost regression model [22] was trained to predict each parameter from the full 15-feature input. Feature relevance was quantified using SHAP [23], and RFE was applied to iteratively remove the least informative features.

The final 8-feature protocol was selected based on: (i) the inflection point in normalized root mean square error (RMSE) across parameters, and (ii) protocol compatibility with time-dependent diffusion kurtosis analysis [38]–[41] for secondary validation of exchange effects.

a) Implementation details: The XGBoost models were trained with 128 trees, a maximum depth of eight, a learning rate of 0.3, a subsampling ratio of 0.6, and an ℓ_2 -regularization coefficient (`lambda`) of 1.0. Training was stopped early if the validation loss failed to improve for 25 consecutive boosting rounds. The one-million synthetic signals were randomly divided into 80% training examples, 10% validation examples, and 10% hold-out test examples. Feature attributions were computed with the tree-SHAP algorithm implemented in the `shap` Python library [23]. Recursive feature elimination proceeded by removing the least important feature at each iteration until only two features remained. We inspected the resulting normalised RMSE curve and retained the eight feature subset located near its inflection point. All scripts, trained models, and the synthetic signal generator are available in the repository cited in the *Data and code availability* section.

F. Comparison of protocol performance

To benchmark the performance and robustness of the XAI-optimized protocol, we evaluated it against the full 15-feature acquisition and two alternative 8-feature subprotocols: one optimized using a traditional FIM framework, and another selected heuristically.

The theory-driven protocol was derived using FIM-based Recursive Feature Elimination (FIM-RFE). Following the D-optimality criterion, which seeks to maximize the determinant of the FIM, the procedure started with the full protocol and iteratively removed the feature whose elimination best preserved the FIM determinant of the remaining subprotocol. The final 8-feature protocol was selected by identifying the point of diminishing returns on the resulting curve.

The naive protocol was designed to reflect a common heuristic approach. It included 8 features with b-values sampled uniformly across the full range at a single diffusion time ($\Delta = 27$ ms), along with three additional b-values ($b = 1$, $b = 2$, and $b = 12.5$ $\text{ms}/\mu\text{m}^2$) acquired at $\Delta = 45$ ms to enable DKI fitting at that Δ and ensure consistency in b-value coverage with the full protocol. This design prioritizes compatibility with other models such as SANDI or time-dependent kurtosis, but results in a more limited Δ range compared to the other protocols.

The comparison across all protocols was multifaceted. In simulations, we assessed the absolute estimation error. For the in vivo data, comparison metrics included the root mean squared deviation (RMSD) of region-of-interest (ROI) medians between protocols, the similarity of parameter distributions across the cortex, and the visual agreement of the resulting cortical surface maps.

Test-retest repeatability was assessed by computing Bland-Altman plots of ROI medians across repeated sessions for each protocol. Limits of agreement and estimation bias were calculated separately for all four NEXI parameters.

III. RESULTS

Figure 1 shows group-averaged cortical maps of NEXI parameters estimated from the full 15-feature protocol. As previously reported [14], [15], [19], elevated values of t_{ex} and f are observed in the sensorimotor cortex, suggesting increased neurite packing and myelination. Interestingly, high t_{ex} values are not observed in visual or temporal regions, unlike prior studies on Connectome 1.0 and Prisma. Our finding for the visual cortex also contrasts with a previous report on the Connectome 2.0 system [19]. Instead, high f values are estimated in the temporal lobe. The intra-neurite diffusivity D_i remains largely homogeneous across the brain, often hitting the enforced upper bound (3.5 $\mu\text{m}^2/\text{ms}$), while D_e is slower in high- f regions, consistent with reduced extracellular space.

To identify a reduced acquisition protocol, we applied a machine learning-based recursive feature elimination strategy using SHAP values computed from XGBoost regressors trained on synthetic NEXI signals. Figure 2 outlines this process. It revealed an inflection point at 7 features in the root mean squared error (RMSE) curves, beyond which additional features yielded marginal improvements (Fig. 2). However, the final protocol retained 8 features, for two main reasons: first, the

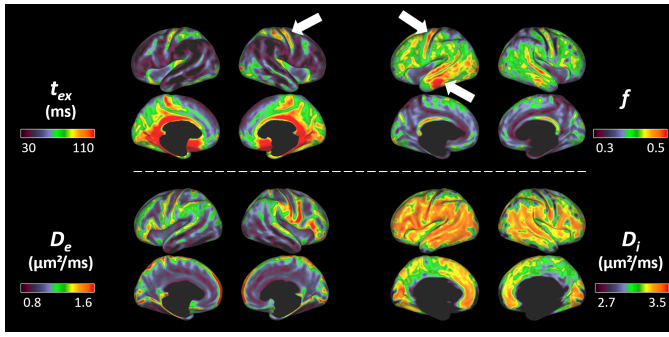


Fig. 1. Cortical surface maps of NEXI parameters from the full protocol. Group-averaged maps of t_{ex} , f , D_i , and D_e across all subjects, displayed on lateral and medial views of both cortical hemispheres. As expected, t_{ex} and f are elevated in the motor cortex, consistent with prior associations to increased myelination and neurite density. However, unlike earlier reports on Connectome 1.0 and Prisma systems, no clear elevation of t_{ex} is observed in the visual cortex or temporal lobe. Interestingly, f is elevated instead in the temporal lobe. In contrast, D_i remains relatively uniform across the cortex ($3 \mu\text{m}^2/\text{ms}$), while D_e appears reduced in areas with high f , potentially reflecting more restricted extracellular environments. These full-protocol maps are used as the spatial reference for evaluating the fidelity of reduced protocols.

inclusion of an additional acquisition ($b=1\text{ms}/\mu\text{m}^2$ at a short Δ) allows for the estimation of diffusion kurtosis at a second diffusion time, thereby enabling time-dependent DKI analysis [38], [41] and a secondary measurement of t_{ex} beyond NEXI; second, repeated iterations of the XAI-RFE process with varying random seeds occasionally indicated an inflection at 8 features, motivating a conservative choice to enhance robustness. The retained features covered a broad range of b -values (1.0 – $12.5 \text{ ms}/\mu\text{m}^2$) and diffusion times (Δ from 15 – 45 ms), ensuring sensitivity to both restricted diffusion and exchange effects.

Validation on 100,000 synthetic noisy signals ($\text{SNR} = 32 \pm 26$ at $b=0$) demonstrated that the XAI-reduced protocol preserves estimation accuracy across the full physiological range of NEXI parameters (Figure 3). A consistent overestimation of t_{ex} is observed for intermediate values, likely related to limited sensitivity at short Δ . D_i tends to be underestimated at intermediate values. Despite this, the reduced protocol shows estimation profiles nearly identical to the full acquisition.

Voxel-level distributions and regional medians in healthy volunteers confirm this consistency (Figure 4). Modes and median values across DKT cortical ROIs show minimal differences between protocols, with t_{ex} around 40 ms , $f \approx 0.36$, and $D_e \approx 0.9 \mu\text{m}^2/\text{ms}$. These results support the robustness of the XAI-reduced protocol across typical inter-subject variability.

In comparison, two alternative subprotocols, one optimized via Fisher Information Matrix (FIM) analysis and one naively sampled, were also evaluated (Figure 5). The FIM-derived protocol includes diverse diffusion times, but its optimization is purely theoretical; it cannot account for how realistic noise actually affects the parameter estimates, and it assumes the information from each measurement point simply adds up, ignoring that some points may be redundant. The naive protocol lacks Δ diversity, reducing sensitivity to exchange. RMSD calculations (Figure 6) show that the XAI-optimized protocol

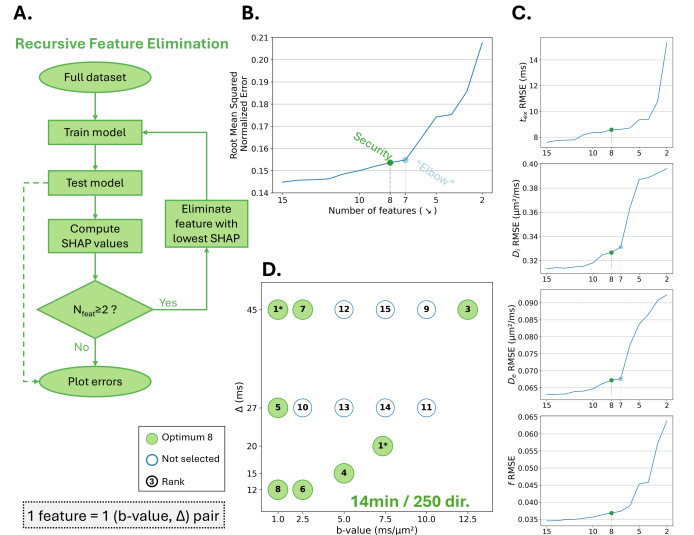


Fig. 2. Recursive feature elimination using SHAP for NEXI protocol optimization. (A.) Overview of the XAI-RFE pipeline: simulated NEXI signals were used to train XGBoost regressors, and SHAP values quantified each feature's contribution to parameter estimation. Features (defined by unique b and Δ values) were iteratively removed based on minimal SHAP importance. Evolution of normalized RMSE across all (B.) and each (C.) parameters as features are removed. An inflection at 7–8 features indicates the minimal protocol length before accuracy sharply degrades. (D.) Visualization of the final selected protocol (green), overlaid on the full 15-feature set. The retained features span both short and long diffusion times and a broad range of b -values.

yields the lowest deviations from the full protocol, particularly for t_{ex} (2.4-fold lower than the naive protocol), f and D_i .

Surface parameter maps further confirm these trends (Figure 7): the XAI protocol closely reproduces spatial contrasts observed in the full protocol, especially elevated t_{ex} and f in sensorimotor and occipital cortices. FIM and naive protocols fail to capture finer gradients and lack fidelity in frontal and temporal areas, especially for f .

Test-retest reproducibility was preserved with the reduced protocol. Bland-Altman analysis (Figure 8) shows that the 8-feature protocol maintains agreement comparable to the full protocol across all parameters, with only marginal increases in the limits of agreement. In comparison, the FIM-reduced and Naive-reduced protocols (See Figure S3) exhibited notably poorer reproducibility, particularly for f where the FIM protocol showed a substantially larger standard deviation in the mean difference compared to the other protocols. This further underscores the superior robustness of the XAI-optimized approach.

We also evaluated the impact of scanner choice and denoising strategy. Cross-scanner comparisons (Supplementary Tables S1 and S2) revealed consistent f and D_e estimates between systems, but longer t_{ex} and elevated D_i values on Connectome 2.0, likely due to increased sensitivity to fast intra-neurite dynamics enabled by higher gradient strength [17]. However, D_i frequently reaches the model's upper bound, raising the possibility of unmodeled soma effects or fit instabilities.

Finally, we assessed the influence of denoising. Although complex MP-PCA denoising offers, in principle, a way to

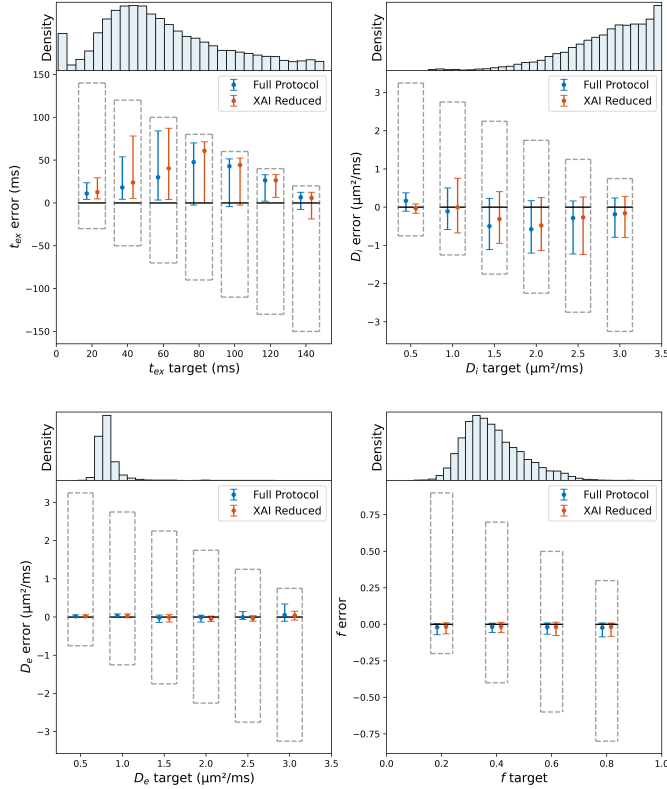


Fig. 3. Estimation error across the parameter space: Full vs. XAI-optimized protocol. Binned error analysis from 100,000 synthetic NEXI signals with added Gaussian noise ($\text{SNR} = 32 \pm 26$), comparing the full protocol (blue) and the reduced 8-feature XAI protocol (orange). For each NEXI parameter (t_{ex} , f , D_i , D_e), absolute estimation errors are plotted as a function of the ground-truth parameter value. Histograms above each panel indicate the distribution of target values in the test set. Error bars represent mean \pm standard deviation within each bin; dashed rectangles denote model fitting bounds. Both protocols show similar error profiles across the full physiological range. A systematic positive bias in t_{ex} is observed, reaching 20-40 ms for intermediate values, likely due to model limitations at short diffusion times or imperfect sensitivity to fast exchange. Estimates of D_i tend to be underestimated at intermediate values. Errors for f and D_e remain low and stable. These results confirm that the XAI-reduced protocol preserves parameter accuracy and robustness under realistic conditions.

avoid Rician floor effects that confound signal interpretation at high b-values, magnitude-based processing with Rician correction currently yielded better model fits (Supplementary Figure S4). This highlights the need for further refinement of complex-domain denoising methods tailored to high-gradient acquisitions.

IV. DISCUSSION

A fundamental barrier hinders the broader adoption of advanced diffusion models: the tension between their biophysical richness and the pragmatic need for time-efficient acquisitions. Optimizing the acquisition time would help promote wider adoption of NEXI in research and clinical applications. For this purpose, we leveraged a state-of-the-art research scanner, the Connectome 2.0, as it offers a unique capability to access a broader range of acquisition parameters enabled by its ultra-high gradient performance. This study

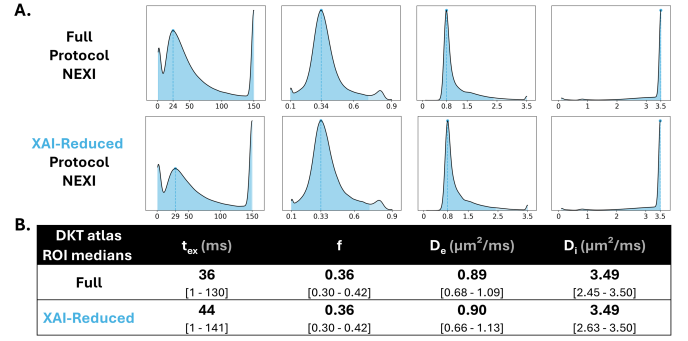


Fig. 4. Distributions and summary of NEXI parameter estimates across DKT cortical regions. (A) Kernel density estimates of voxel-level values for each NEXI parameter (t_{ex} , f , D_e , D_i), aggregated across all DKT ROIs and all subjects. The full protocol (top row) and XAI-reduced protocol (bottom row) yield very similar distributions. The vertical dashed lines indicate the mode of each distribution, reflecting the most frequent voxel value. Both protocols exhibit similar features: a strong ceiling effect for D_i at the upper model bound ($3.5 \mu\text{m}^2/\text{ms}$), right-skewed t_{ex} distributions with local peaks around 25-30 ms, and unimodal distributions for f and D_e . (B) Summary statistics computed from ROI-wise medians across the cortex. Median values and ranges are consistent between protocols, confirming the robustness of the XAI-reduced protocol.

successfully demonstrates the feasibility of robustly estimating Neurite Exchange Imaging (NEXI) parameters in human cortical gray matter using a substantially reduced diffusion MRI protocol consisting of only eight strategically selected (b , Δ) combinations. Leveraging a data-driven optimization framework based on explainable machine learning (XGBoost-SHAP-RFE or XAI), we achieved a two-fold reduction in scan time on the Connectome 2.0 platform, from 27 to 14 minutes, while preserving key features of spatial contrast, parameter accuracy, and test-retest reproducibility. These findings provide a critical advancement toward the clinical and translational implementation of exchange-sensitive diffusion models, particularly in cortical regions where scan time constraints, noise susceptibility, and parameter degeneracy have traditionally hindered adoption.

A. Advantages of SHAP-guided empirical protocol reduction

The primary methodological contribution of this study lies in the use of SHAP-guided RFE to empirically optimize a heuristically designed diffusion protocol design. Unlike conventional approaches based on the FIM or theoretical parameter identifiability under Gaussian noise assumptions [20], [21], our method operates without relying on a purely theoretical framework. While some studies have extended the FIM to Rician noise [42], this method would still operate within a fully theoretical framework. Our approach, by contrast, is a data-driven alternative that directly integrates the combined effects of realistic noise, model degeneracy, and signal correlations, as observed in our dataset, into the feature selection process. The SHAP-RFE framework's analysis revealed that the most informative features are located at the extremes of the (b , Δ) acquisition space. This is consistent with the need to sample a wide range of physical regimes to accurately constrain the

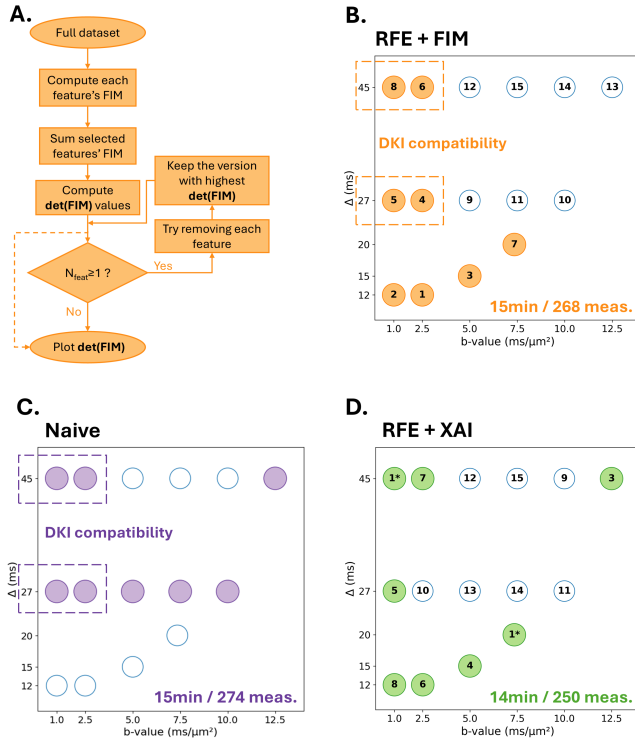


Fig. 5. Comparison of reduced protocols: FIM-optimized vs. naive. (A) Schematic of the Fisher Information Matrix (FIM)-based Recursive Feature Elimination (FIM-RFE) algorithm. At each step, all possible subprotocols with one fewer feature are evaluated, and the one yielding the highest $\log \det(\text{FIM})$ is retained. The process is repeated until only a single feature remains, and the curve of $\log \det(\text{FIM})$ vs. number of features is plotted. (B) The FIM-optimized protocol selected via this method includes 8 features that span a wide range of b -values and diffusion times, including short Δ values, thus maintaining sensitivity to fast exchange processes. Several pairs of features also ensure compatibility with time-dependent diffusion kurtosis analyses. (C) The naive protocol includes 8 features sampled uniformly across b -values at two fixed diffusion times ($\Delta = 27$ ms and $\Delta = 45$ ms), emphasizing time-dependant kurtosis analysis compatibility and at least one Δ with many b -values as a multi-shell protocol (e.g. for Standard Model or SANDI compatibility). The limited range in diffusion times may however reduce sensitivity to rapid exchange dynamics.

biophysical model and prevent parameter degeneracy. This distinction proved crucial: the FIM-optimized protocol, though theoretically well-conditioned, failed to preserve parameter distributions and spatial patterns, particularly for t_{ex} and f . This was because, unlike our XAI-driven approach, the FIM failed to capture the importance of including the longest diffusion time with the strongest b -value. This specific data point, which proved crucial for the accurate estimation of these parameters, was correctly identified as essential by our methodology.

By contrast, our SHAP-RFE framework, trained on synthetic NEXI signals spanning the full physiological range and realistic SNR regimes, yielded a reduced protocol that consistently outperformed both FIM and naive subsampling approaches. This data-driven approach was chosen because it allows for a comprehensive and uniform sampling of the NEXI parameter space, which is critical for robust and unbiased training of the XGBoost regressor. The selected features span the full b -value range and preserve all Δ values, supporting estimation

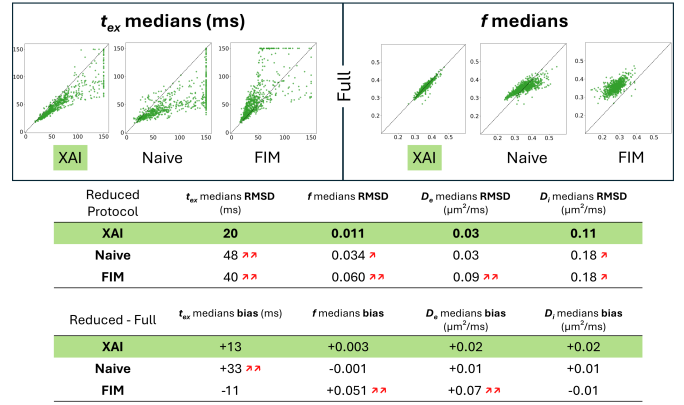


Fig. 6. Root Mean Square Deviation (RMSD) and estimation bias of NEXI parameters across protocols. Each point corresponds to the RMSD between the median value from the full protocol and that from a reduced subprotocol (XAI-optimized, FIM, or naive) within a specific DKT ROI for a given subject, aggregated across all ROIs and subjects. RMSD and median bias values for all NEXI parameters (t_{ex} , f , D_e , D_i) are presented for the XAI-optimized, Naive, and FIM protocols relative to the full protocol. Values in bold indicate the lowest RMSD, while red arrows denote an increase in RMSD or bias compared to the XAI protocol. The XAI-optimized protocol consistently shows the lowest deviation (RMSD) and low bias across parameters, with a 2.4-fold lower RMSD in t_{ex} compared to the naive protocol. These results confirm that the data-driven XAI selection strategy yields better preservation of parameter estimates and reduces bias more effectively than both theoretical (FIM) and heuristic (naive) subsampling approaches.

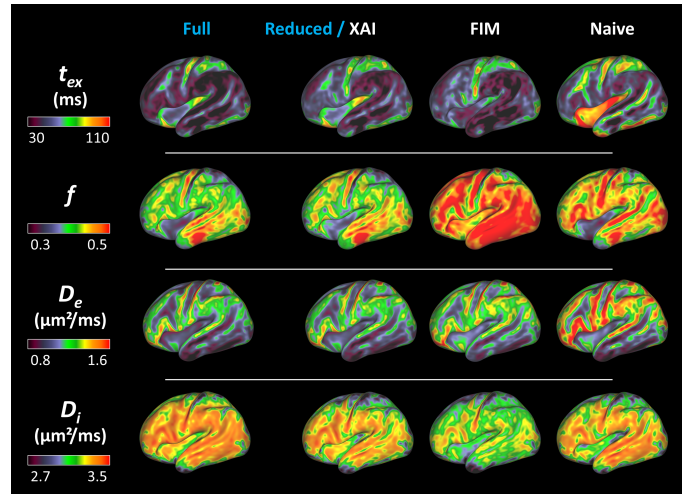


Fig. 7. Left hemisphere cortical maps of NEXI parameters across all acquisition protocols. Group-averaged cortical surface maps for t_{ex} , f , D_e , and D_i are shown for four protocols: Full, XAI-optimized (SHAP-based), FIM-optimized, and naive. While all protocols capture general spatial trends, the XAI protocol best reproduces the contrasts seen in the full protocol, particularly elevated t_{ex} and f in sensorimotor and occipital cortices. The FIM and naive protocols fail to preserve finer gradients and exaggerate parameter ranges in frontal and temporal areas, especially for f and t_{ex} , likely due to limited range in either b or Δ values. Across all protocols, D_i remains consistently high and spatially homogeneous, while D_e shows local reduction in sensorimotor regions. These results underscore the importance of informed protocol selection for maintaining microstructural interpretability in cortical NEXI mapping.

of time-dependent kurtosis. Notably, these combinations would be difficult to derive from intuition or analytic simplifications

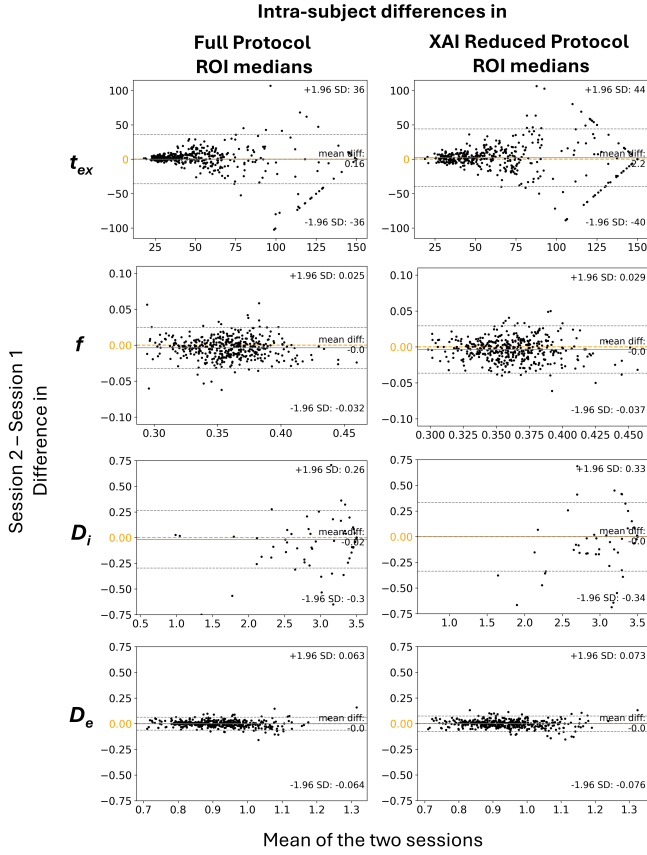


Fig. 8. Test-retest reproducibility of NEXI estimates using the full protocol and the XAI-optimized subprotocol. Bland-Altman plots show intra-subject variability across scan-rescan sessions, using DKT ROI median values for each NEXI parameter (t_{ex} , f , D_i , D_e). Left: Full protocol. Right: XAI-Reduced protocol. Each plot displays the difference between sessions against their mean, with orange lines indicating bias and dotted gray lines denoting the 95% limits of agreement. The XAI protocol maintains reproducibility comparable to the full protocol, with marginally wider limits for t_{ex} and D_i but near-identical performance for f and D_e . This supports the use of the 8-feature reduced protocol in longitudinal studies where acquisition time is constrained.

alone.

Our results confirm and extend the utility of SHAP-based RFE pipelines previously applied in other biomedical contexts [24], [25], [27]. In particular, similar approaches using XGBoost-SHAP-RFE for feature pruning in physiological state classification [26], symptom triage [25], and environmental sensor optimization [27] have demonstrated strong generalization under high-dimensional, noisy conditions or characteristics shared with diffusion MRI signal modeling.

In our context, the XGBoost-SHAP-RFE optimization led to a consistent inflection point at 7-8 features, beyond which accuracy gains plateaued (Fig. 2). Retaining 8 features ensured coverage of both short and long diffusion times, and allowed compatibility with secondary metrics such as time-dependent diffusion kurtosis [43]. Critically, the final protocol not only reproduced parameter estimates, but also preserved cortical contrast patterns observed in full acquisitions, including elevated t_{ex} and f in sensorimotor cortex [14], [19].

B. Reproducibility and generalization of the reduced protocol

Beyond estimation accuracy, test-retest reproducibility is essential for longitudinal studies, particularly when subtle microstructural changes are of interest. We found that the XAI-reduced protocol maintained intra-subject consistency across repeated scans, with only marginal increases in limits of agreement for t_{ex} and D_i compared to the full protocol (Fig. 8). This aligns with prior findings that exchange-related metrics display moderate SNR sensitivity [10], [14], but confirms that performance remains within within ranges reported in prior studies on clinical and research scanners [14], [15], [19].

Furthermore, the protocol’s robustness was confirmed in an exploratory high-resolution acquisition, demonstrating its potential to reduce partial volume effects (PVE) in cortical gray matter (see Supplementary Figures S5 and S6).

Together, these results validate the use of explainable machine learning not merely as a black-box tool, but as a transparent and interpretable strategy for optimizing biophysically-informed acquisition design. The flexibility of our framework allows retraining under alternative models (e.g., SMEX [13], GEM [44]), scanner configurations, or populations of interest, thereby supporting future clinical translation and cross-site harmonization efforts.

C. Spatial specificity and reproducibility across the cortical ribbon

The spatial distributions of NEXI parameters obtained from the XAI-optimized protocol closely match those observed with the full acquisition, demonstrating that a data-driven subprotocol can preserve biologically relevant contrasts across the cortex. Elevated t_{ex} and f in sensorimotor cortex, previously linked to dense myelination and high neurite packing [14], [15], [19], were clearly recapitulated. Interestingly, our data partially diverged from earlier studies by showing moderate t_{ex} in visual cortex. This discrepancy may reflect increased sensitivity to fast exchange enabled by the short diffusion times of Connectome 2.0 ($\Delta = 15 - 45$ ms, $\delta = 5$ ms) [17], [19]. We also observed unexpectedly higher f values in temporal regions, despite prior reports associating the temporal lobe with lower cellular and axonal density [45], and previous NEXI maps consistently showing the opposite trend in this region [14], [15], [19]. This may be explained by the lower SNR in these regions, which qualitatively affects the robustness of the parameter estimation.

In terms of estimation accuracy, the XAI-optimized protocol demonstrated a substantial improvement over the alternative schemes. RMSD calculations showed that the XAI protocol yielded a 2 and 2.4-fold lower RMSD in t_{ex} compared to the FIM and naive protocol respectively, and consistently showed a lower RMSD and bias across all parameters compared to the alternative schemes (Figure 6). Importantly, test-retest analyses (Fig. 8) confirm that this compact protocol retains measurement reliability for longitudinal studies and sensitivity to between-subject differences. While t_{ex} and D_i showed marginally broader limits of agreement, their reproducibility remained within ranges reported in previous Connectome and Prisma

studies [14], [15]. The stability of f and D_e was particularly robust, supporting the feasibility of deploying this protocol in clinical cohorts where subject motion or compliance imposes strict scan-time constraints.

D. Limits of model fidelity and parameter identifiability

Our analysis also underscores persistent challenges in NEXI parameter estimation. Specifically, D_i often hits its upper model bound ($3.5 \mu\text{m}^2/\text{ms}$), a behavior also noted in prior work on white matter models like NODDI [46], [47] and in recent cortical applications of NEXI [14], suggesting that this lack of sensitivity to high intra-neurite diffusivity is a general feature of multi-compartment diffusion models. Similar concerns apply to t_{ex} estimation, where we observe systematic overestimation at intermediate values (Fig. 3), likely arising from the interplay between limited short- Δ data and degeneracy in the fitting landscape.

Such biases raise important considerations for model selection and parameter interpretation. As shown in both simulation and experimental studies, models that neglect Rician noise can overestimate t_{ex} [14], [19]. Similarly, failing to account for the finite duration of gradient pulses, an issue addressed by models like SMEX [13], can also lead to unrealistically high D_i estimates [15]. Furthermore, other unmodeled factors, such as contributions from cell somas or structural disorder, can also introduce biases in the estimation of D_i , f and even t_{ex} [12], [48]. These observations echo similar issues reported in white matter modeling [46], [49] and point toward the need for more comprehensive signal models capable of handling gray matter complexity.

E. Denoising tradeoffs and noise-model mismatch

Another key finding relates to the influence of signal-domain processing. Despite theoretical optimality, complex-valued MP-PCA denoising with Gaussian noise assumptions resulted in poorer model fits at high b-values than magnitude-domain denoising followed by Rician bias correction (Fig. S4), a result also seen in [14]. This may reflect residual violations of noise model assumptions, especially in regions with low SNR or spatially correlated noise, arising from different reconstruction steps such as coil combination and parallel imaging [50].

Future studies may benefit from incorporating more advanced denoising strategies, such as NORDIC [51] or denoising models with spatially varying noise priors [50], tailored specifically for cortical data. The possibility of using real-valued reconstructions to suppress Rician floor effects while preserving SNR remains a promising avenue for enhancing estimation robustness.

F. Clinical translation and cross-platform generalizability

While the proposed 8-feature protocol performs robustly on Siemens Connectome 2.0, its direct deployment on most clinical MRI systems is limited by hardware constraints. For example, Siemens Prisma-class scanners (maximum 80 mT/m) require longer δ and Δ to reach high b-values, reducing sensitivity to short-time exchange processes and violating the NPA that

underlies the NEXI model. However, the emergence of clinical-grade scanners with ultra-high gradient performance, such as the GE Magnus (300 mT/m, 750 T/m/s) or the Siemens Cima.X (200 mT/m, 200 T/m/s), presents new opportunities. These systems are capable of running protocols similar to the one we’ve optimized, demonstrating that our data-driven approach is broadly applicable and not limited to a single research scanner. Prior work has shown that on standard clinical scanners, the SMEX model, which integrates full gradient waveforms, yields more accurate estimates [13], [15].

Nevertheless, the XGBoost-SHAP-RFE optimization framework introduced here can be readily adapted to generate optimized subprotocols under these constraints. By re-training the XGBoost regressors on synthetic signals generated with Prisma-specific pulse timings and noise characteristics, it is possible to derive context-appropriate protocols that preserve the strengths of our approach while ensuring model validity. One of our previous works already begun applying SHAP-based optimization for clinical NEXI acquisition [52], and our new findings further validate the utility of this pipeline for rapid, interpretable protocol design.

G. Toward multi-model and population-specific optimization

Finally, we note that the SHAP-RFE approach is model-agnostic and supports extensions beyond NEXI. As the field moves toward multi-compartment models that incorporate soma (e.g., SANDIX) [13], [44], structural disorder [48], or relaxation [12], protocol optimization strategies must evolve accordingly. Our method provides a principled route for empirically selecting features that maximize sensitivity across competing models or prioritize specific biological hypotheses. For instance, this approach could inform the development of free-waveform protocols aiming to enhance sensitivity to both cortical exchange and restriction, complementing existing frameworks such as that of Chakwizira et al. [53].

Furthermore, future work may incorporate priors from pathology-specific cohorts or link optimization targets to downstream biomarkers (e.g., myelin water fraction, cortical thinning, clinical scores). The interpretability and modularity of SHAP facilitate such integration, offering an avenue for personalized or disease-aware protocol design that bridges methodological rigor with translational relevance. Beyond this, our optimization framework could be extended to other acquisition dimensions. For instance, future work could aim to optimize the number of diffusion directions per (b, Δ) combination. This would require a different pipeline than the one used for feature elimination, as simply removing a direction adds noise to the corresponding data point, which could bias the importance ranking and lead to unstable results.

Taken together, our findings demonstrate that XGBoost-SHAP-RFE-based protocol optimization is a powerful and adaptable tool for accelerating diffusion MRI acquisitions while preserving biological specificity. By empirically identifying informative (b, Δ) pairs under realistic noise and model uncertainty, we provide a scalable framework for optimizing complex

biophysical imaging protocols. This framework is generalizable to other scanner platforms, populations, and research questions, and our work represents a key first step towards its broader application. It contributes a key advancement toward the widespread deployment of exchange-sensitive microstructural imaging in research and clinical applications.

V. CONCLUSION

We present a data-driven protocol optimization framework for Neurite Exchange Imaging (NEXI), leveraging explainable machine learning to identify a compact 8-feature acquisition scheme that maintains estimation accuracy, spatial specificity, and repeatability. Applied on the Connectome 2.0 platform, this reduced protocol cuts scan time nearly by half compared to the full 15-feature reference, while outperforming both Fisher Information Matrix-based and naive subsampling strategies.

Our results confirm that empirical feature selection guided by model prediction behavior under noise can surpass classical theoretical approaches, particularly for challenging parameters like t_{ex} and f . The optimized protocol preserves group-level trends and supports high-resolution imaging.

While not directly portable to clinical systems due to gradient constraints, the proposed optimization method can be retrained for such platforms using realistic simulations. This flexible framework represents a critical step toward clinically viable, exchange-sensitive dMRI protocols for probing cortical microstructure in vivo.

DATA AND CODE AVAILABILITY

The code used in this study is available at https://github.com/Mic-map/graymatter_swissknife. All code for XGBoost-SHAP-RFE optimisation is publicly available at <https://github.com/QuentinUhl/XAI-dMRI-protocol-optimization>. The data that support the findings of this study are available from the corresponding author upon reasonable request.

REFERENCES

- [1] J. W. Dong, I. O. Jelescu, B. Ades-Aron, D. S. Novikov, K. Friedman, J. S. Babb, R. S. Osorio, J. E. Galvin, T. M. Shepherd, and E. Fieremans, "Diffusion MRI biomarkers of white matter microstructure vary nonmonotonically with increasing cerebral amyloid deposition," *Neurobiology of Aging*, vol. 89, pp. 118–128, May 2020.
- [2] C. Atkinson-Clement, S. Pinto, A. Eusebio, and O. Coulon, "Diffusion tensor imaging in Parkinson's disease: Review and meta-analysis," *NeuroImage: Clinical*, vol. 16, pp. 98–110, Jan. 2017.
- [3] N. Spotorno, O. Strandberg, G. Vis, E. Stomrud, M. Nilsson, and O. Hansson, "Measures of cortical microstructure are linked to amyloid pathology in Alzheimer's disease," *Brain*, vol. 146, no. 4, pp. 1602–1614, Apr. 2023.
- [4] P. J. Basser, J. Mattiello, and D. LeBihan, "Estimation of the Effective Self-Diffusion Tensor from the NMR Spin Echo," *Journal of Magnetic Resonance, Series B*, vol. 103, no. 3, pp. 247–254, Mar. 1994.
- [5] D. Le Bihan, R. Turner, C. T. W. Moonen, and J. Pekar, "Imaging of diffusion and microcirculation with gradient sensitization: Design, strategy, and significance," *Journal of Magnetic Resonance Imaging*, vol. 1, no. 1, pp. 7–28, Jan. 1991.
- [6] D. C. Alexander, T. B. Dyrby, M. Nilsson, and H. Zhang, "Imaging brain microstructure with diffusion MRI: Practicality and applications," *NMR in Biomedicine*, vol. 32, no. 4, p. e3841, 2019, e3841 NBM-16-0261.R1.
- [7] I. O. Jelescu, M. Palombo, F. Bagnato, and K. G. Schilling, "Challenges for biophysical modeling of microstructure," *Journal of Neuroscience Methods*, vol. 344, p. 108861, Oct. 2020.
- [8] D. S. Novikov, E. Fieremans, S. N. Jespersen, and V. G. Kiselev, "Quantifying brain microstructure with diffusion MRI: Theory and parameter estimation," *NMR in Biomedicine*, vol. 32, no. 4, p. e3998, 2019.
- [9] G. J. Stanisz, G. A. Wright, R. M. Henkelman, and A. Szafer, "An analytical model of restricted diffusion in bovine optic nerve," *Magnetic Resonance in Medicine*, vol. 37, no. 1, pp. 103–111, 1997.
- [10] I. O. Jelescu, A. de Skowronski, F. Geffroy, M. Palombo, and D. S. Novikov, "Neurite Exchange Imaging (NEXI): A minimal model of diffusion in gray matter with inter-compartment water exchange," *NeuroImage*, vol. 256, p. 119277, Aug. 2022.
- [11] M. Palombo, A. Ianus, M. Guerreri, D. Nunes, D. C. Alexander, N. Shemesh, and H. Zhang, "SANDI: A compartment-based model for non-invasive apparent soma and neurite imaging by diffusion MRI," *NeuroImage*, vol. 215, p. 116835, Jul. 2020.
- [12] H.-H. Lee, A. Papaioannou, D. S. Novikov, and E. Fieremans, "In vivo observation and biophysical interpretation of time-dependent diffusion in human cortical gray matter," *NeuroImage*, vol. 222, p. 117054, Nov. 2020.
- [13] J. L. Olesen, L. Østergaard, N. Shemesh, and S. N. Jespersen, "Diffusion time dependence, power-law scaling, and exchange in gray matter," *NeuroImage*, vol. 251, p. 118976, May 2022.
- [14] Q. Uhl, T. Pavan, M. Molendowska, D. K. Jones, M. Palombo, and I. O. Jelescu, "Quantifying human gray matter microstructure using neurite exchange imaging (NEXI) and 300 mT/m gradients," *Imaging Neuroscience*, vol. 2, pp. 1–19, Mar. 2024.
- [15] Q. Uhl, T. Pavan, T. Feiweier, G. F. Piredda, and I. Jelescu, "Human gray matter microstructure mapped using neurite exchange imaging (NEXI) on a clinical scanner," *Imaging Neuroscience*, vol. 3, p. IMAG.a.32, Jun. 2025.
- [16] I. Illán-Gala, V. Montal, S. Borrego-Écija, M. L. Mandelli, N. Falgàs, A. E. Welch, J. Pegueroles, M. Santos-Santos, A. Bejanin, D. Alcolea, O. Dols-Icardo, O. Belbin, M. B. Sánchez-Saudinós, N. Bargalló, S. González-Ortiz, A. Lladó, R. Blesa, B. C. Dickerson, H. J. Rosen, B. L. Miller, A. Lleó, M. L. Gorno-Tempini, R. Sánchez-Valle, and J. Fortea, "Cortical microstructure in primary progressive aphasia: A multicenter study," *Alzheimer's Research & Therapy*, vol. 14, no. 1, p. 27, Feb. 2022.
- [17] S. Y. Huang, T. Witzel, B. Keil, A. Scholz, M. Davids, P. Dietz, E. Rummert, R. Ramb, J. E. Kirsch, A. Yendiki, Q. Fan, Q. Tian, G. Ramos-Llorden, H.-H. Lee, A. Nummenmaa, B. Bilgic, K. Setsompop, F. Wang, A. V. Avram, M. Komlosch, D. Benjamini, K. N. Magdoo, S. Pathak, W. Schneider, D. S. Novikov, E. Fieremans, S. Tounekti, C. Mekkaoui, J. Augustinack, D. Berger, A. Shapson-Coe, J. Lichtman, P. J. Basser, L. L. Wald, and B. R. Rosen, "Connectome 2.0: Developing the next-generation ultra-high gradient strength human MRI scanner for bridging studies of the micro-, meso- and macro-connectome," *NeuroImage*, vol. 243, p. 118530, Nov. 2021.
- [18] G. Ramos-Llorden, H.-H. Lee, M. Davids, P. Dietz, A. Krug, J. E. Kirsch, M. Mahmutovic, A. Müller, Y. Ma, H. Lee, C. Maffei, A. Yendiki, B. Bilgic, D. J. Park, Q. Tian, B. Clifford, W.-C. Lo, S. Stocker, J. Fischer, G. Ruyters, M. Roesler, A. Potthast, T. Benner, E. Rummert, R. Schuster, P. J. Basser, T. Witzel, L. L. Wald, B. R. Rosen, B. Keil, and S. Y. Huang, "Ultra-high gradient connectomics and microstructure MRI scanner for imaging of human brain circuits across scales," *Nature Biomedical Engineering*, pp. 1–16, Jul. 2025.
- [19] K.-S. Chan, Y. Ma, H. Lee, J. P. Marques, J. L. Olesen, S. Coelho, D. S. Novikov, S. N. Jespersen, S. Y. Huang, and H.-H. Lee, "In vivo human neurite exchange time imaging at 500 mT/m diffusion gradients," *Imaging Neuroscience*, Apr. 2025.
- [20] O. Jalnefjord, M. Montelius, G. Starck, and M. Ljungberg, "Optimization of b-value schemes for estimation of the diffusion coefficient and the perfusion fraction with segmented intravoxel incoherent motion model fitting," *Magnetic Resonance in Medicine*, vol. 82, no. 4, pp. 1541–1552, Oct. 2019.
- [21] P. Flaherty, A. Arkin, and M. Jordan, "Robust design of biological experiments," in *Advances in Neural Information Processing Systems*, vol. 18. MIT Press, 2005.
- [22] T. Chen and C. Guestrin, "XGBoost: A scalable tree boosting system," in *Proceedings of the 22nd ACM SIGKDD International Conference on Knowledge Discovery and Data Mining*, ser. Kdd '16. San Francisco, California, USA and New York, NY, USA: Association for Computing Machinery, 2016, pp. 785–794.
- [23] S. M. Lundberg and S.-I. Lee, "A unified approach to interpreting model predictions," in *Advances in Neural Information Processing Systems*, I. Guyon, U. V. Luxburg, S. Bengio, H. Wallach, R. Fergus, S. Vishwanathan, and R. Garnett, Eds., vol. 30. Curran Associates, Inc., 2017, pp. 4768–4777.

- [24] J. Zhu, Z. Zhao, C. Wu, C. Yin, R. Chen, and Y. Ding, "An integrated approach of feature selection and machine learning for early detection of breast cancer," *Scientific Reports*, vol. 15, no. 1, p. 13015, Apr. 2025.
- [25] J. Rufino, J. M. Ramírez, J. Aguilar, C. Baquero, J. Champati, D. Frey, R. E. Lillo, and A. Fernández-Anta, "Performance and explainability of feature selection-boosted tree-based classifiers for COVID-19 detection," *Heliyon*, vol. 10, no. 1, p. e23219, Jan. 2024.
- [26] J. Huang, Y. Peng, and L. Hu, "A multilayer stacking method base on RFE-SHAP feature selection strategy for recognition of driver's mental load and emotional state," *Expert Systems with Applications*, vol. 238, p. 121729, Mar. 2024.
- [27] L. Wang, L. Dong, and Q. Zhang, "Coupling Interpretable Feature Selection with Machine Learning for Evapotranspiration Gap Filling," *Water*, vol. 17, no. 5, p. 748, Jan. 2025.
- [28] U. Ahmed, Z. Jiangbin, A. Almogren, M. Sadiq, A. U. Rehman, M. T. Sadiq, and J. Choi, "Hybrid bagging and boosting with SHAP based feature selection for enhanced predictive modeling in intrusion detection systems," *Scientific Reports*, vol. 14, no. 1, p. 30532, Dec. 2024.
- [29] O. Chernyaeva and T. Hong, "Prediction of Customer Satisfaction Using RFE-SHAP Feature Selection Method," *Journal of Intelligence and Information Systems*, vol. 29, no. 4, pp. 325–345, 2023.
- [30] M. Mahmutovic, M. Shrestha, G. Ramos-Llordén, D. Sung, L. J. Edwards, Y. Chu, P. I. Dubovan, A. Müller, S.-L. J. Hansen, A. Ghotra, K. J. Pine, R. Müller, N. Weiskopf, L. L. Wald, C. Mekkaoui, H. E. Möller, S. Y. Huang, and B. Keil, "High-density MRI coil arrays with integrated field monitoring systems for human connectome mapping," *Magnetic Resonance in Medicine*, vol. 94, no. 5, pp. 2286–2303, 2025.
- [31] J. Veraart, D. S. Novikov, D. Christiaens, B. Ades-aron, J. Sijbers, and E. Fieremans, "Denoising of diffusion MRI using random matrix theory," *NeuroImage*, vol. 142, pp. 394–406, Nov. 2016.
- [32] E. Kellner, B. Dhital, V. G. Kiselev, and M. Reisert, "Gibbs-ringing artifact removal based on local subvoxel-shifts," *Magnetic Resonance in Medicine*, vol. 76, no. 5, pp. 1574–1581, Nov. 2016.
- [33] J. L. R. Andersson and S. N. Sotiropoulos, "An integrated approach to correction for off-resonance effects and subject movement in diffusion MR imaging," *NeuroImage*, vol. 125, pp. 1063–1078, Jan. 2016.
- [34] L. Henschel, S. Conjeti, S. Estrada, K. Diers, B. Fischl, and M. Reuter, "FastSurfer - A fast and accurate deep learning based neuroimaging pipeline," *NeuroImage*, vol. 219, p. 117012, Oct. 2020.
- [35] A. Klein and J. Tourville, "101 Labeled Brain Images and a Consistent Human Cortical Labeling Protocol," *Frontiers in Neuroscience*, vol. 6, 2012.
- [36] B. Avants, N. J. Tustison, and G. Song, "Advanced Normalization Tools: V1.0," *The Insight Journal*, Jul. 2009.
- [37] D. Marcus, J. Harwell, T. Olsen, M. Hodge, M. Glasser, F. Prior, M. Jenkinson, T. Laumann, S. Curtiss, and D. Van Essen, "Informatics and Data Mining Tools and Strategies for the Human Connectome Project," *Frontiers in Neuroinformatics*, vol. 5, 2011.
- [38] E. Fieremans, D. S. Novikov, J. H. Jensen, and J. A. Helpert, "Monte Carlo study of a two-compartment exchange model of diffusion," *NMR in Biomedicine*, vol. 23, no. 7, pp. 711–724, 2010.
- [39] M. Aggarwal, M. D. Smith, and P. A. Calabresi, "Diffusion-time dependence of diffusional kurtosis in the mouse brain," *Magnetic Resonance in Medicine*, vol. 84, no. 3, pp. 1564–1578, 2020.
- [40] E. Solomon, G. Lemberskiy, S. Baete, K. Hu, D. Malyarenko, S. Swanson, A. Shukla-Dave, S. E. Russek, E. Zan, and S. G. Kim, "Time-dependent diffusivity and kurtosis in phantoms and patients with head and neck cancer," *Magnetic Resonance in Medicine*, vol. 89, no. 2, pp. 522–535, Feb. 2023.
- [41] D. S. Novikov, E. Fieremans, J. H. Jensen, and J. A. Helpert, "Time-Dependent Diffusion & Kurtosis as a Probe of Tissue Structure," in *Proc. Intl. Soc. Mag. Reson. Med. 2011*, Montreal, 2011, p. 1988.
- [42] O. T. Karlsen, R. Verhagen, and W. M. Bovée, "Parameter estimation from Rician-distributed data sets using a maximum likelihood estimator: Application to t1 and perfusion measurements," *Magnetic Resonance in Medicine*, vol. 41, no. 3, pp. 614–623, 1999.
- [43] R. N. Henriques, S. N. Jespersen, and N. Shemesh, "Microscopic anisotropy misestimation in spherical-mean single diffusion encoding MRI," *Magnetic resonance in medicine*, vol. 81, no. 5, pp. 3245–3261, 2019.
- [44] Q. Uhl, T. Pavan, I. de Riedmatten, J. Nguyen-Duc, and I. Jelescu, "GEM: A unifying model for Gray Matter microstructure," in *Proc. Intl. Soc. Mag. Reson. Med. 2024*, Singapore, Singapore, 2024, p. 3455.
- [45] P. F. M. Ribeiro, L. Ventura-Antunes, M. Gabi, B. Mota, L. T. Grinberg, J. M. Farfel, R. E. L. Ferretti-Rebustini, R. E. P. Leite, W. J. Filho, and S. Herculanou-Houzel, "The human cerebral cortex is neither one nor many: Neuronal distribution reveals two quantitatively different zones in the gray matter, three in the white matter, and explains local variations in cortical folding," *Frontiers in Neuroanatomy*, vol. 7, p. 28, Sep. 2013.
- [46] I. O. Jelescu, J. Veraart, E. Fieremans, and D. S. Novikov, "Degeneracy in model parameter estimation for multi-compartmental diffusion in neuronal tissue: Degeneracy in Model Parameter Estimation of Diffusion in Neural Tissue," *NMR in Biomedicine*, vol. 29, no. 1, pp. 33–47, Jan. 2016.
- [47] A. F. Howard, M. Cottaar, M. Drakesmith, Q. Fan, S. Y. Huang, D. K. Jones, F. J. Lange, J. Mollink, S. U. Rudrapatna, Q. Tian, K. L. Miller, and S. Jbabdi, "Estimating axial diffusivity in the NODDI model," *NeuroImage*, vol. 262, p. 119535, Nov. 2022.
- [48] D. S. Novikov, R. Coronado-Leija, and E. Fieremans, "Exchange between structurally-disordered compartments," in *Proc. Intl. Soc. Mag. Reson. Med. 2023*, Toronto, Canada, 2023, p. 0684.
- [49] B. Dhital, M. Reisert, E. Kellner, and V. G. Kiselev, "Intra-axonal diffusivity in brain white matter," *NeuroImage*, vol. 189, pp. 543–550, Apr. 2019.
- [50] R. N. Henriques, A. Ianuş, L. Novello, J. Jovicich, S. N. Jespersen, and N. Shemesh, "Efficient PCA denoising of spatially correlated redundant MRI data," *Imaging Neuroscience*, vol. 1, pp. 1–26, Dec. 2023.
- [51] S. Moeller, P. K. Pisharady, S. Ramanna, C. Lenglet, X. Wu, L. Dowdle, E. Yacoub, K. Uğurbil, and M. Akçakaya, "NOise reduction with Distribution Corrected (NORDIC) PCA in dMRI with complex-valued parameter-free locally low-rank processing," *NeuroImage*, vol. 226, p. 117539, Feb. 2021.
- [52] Q. Uhl, T. Pavan, T. Feiweier, E. J. Canales-Rodríguez, and I. O. Jelescu, "Optimizing the NEXI acquisition protocol for quantifying human gray matter microstructure on a clinical MRI scanner using Explainable AI," in *Proc. Intl. Soc. Mag. Reson. Med. 2023*, Toronto, Canada, Jun. 2023, p. 0948.
- [53] A. Chakwizira, A. Zhu, T. Foo, C.-F. Westin, F. Szczepankiewicz, and M. Nilsson, "Diffusion MRI with free gradient waveforms on a high-performance gradient system: Probing restriction and exchange in the human brain," *NeuroImage*, vol. 283, p. 120409, Dec. 2023.

Explainable AI for Accelerated Microstructure Imaging: A SHAP-Guided Protocol on the Connectome 2.0 scanner

Quentin Uhl¹, Tommaso Pavan¹, Julianna Gerold¹, Kwok-Shing Chan¹, Yohan Jun¹, Shohei Fujita¹, Aneri Bhatt¹, Yixin Ma¹, Qiaochu Wang¹, Hong-Hsi Lee¹, Susie Y. Huang¹, Berkin Bilgic¹, and Ileana Jelescu¹

SUPPLEMENTARY MATERIALS

This work was supported in part by the Swiss National Science Foundation (SNSF) under Eccellenza grant PCEFP2_194260 and an SNSF Mobility Grant; by the National Institutes of Health (NIH) under grants R01 EB028797, R01 EB032378, R01 EB034757, R21 AG082377, R21 EB036105, P41 EB030006, U01 EB026996, and UG3 EB034875; and by NWO/ZonMw under Rubicon award 04520232330012. (Corresponding author: Quentin Uhl, e-mail: quentin.uhl@chuv.ch.)

Q. Uhl, T. Pavan, and I. Jelescu are with the Department of Radiology, Lausanne University Hospital (CHUV) and University of Lausanne, Lausanne, 1011, Switzerland (e-mail: quentin.uhl@chuv.ch; tommaso.pavan@chuv.ch; ileana.jelescu@chuv.ch).

Q. Wang is with the École Polytechnique Fédérale de Lausanne (EPFL), Lausanne, 1015, Switzerland (e-mail: qiaochu.wang@epfl.ch).

J. Gerold, K.-S. Chan, Y. Jun, S. Fujita, A. Bhatt, Y. Ma, H.-H. Lee, S. Y. Huang, and B. Bilgic are with the Department of Radiology, Massachusetts General Hospital, Athinoula A. Martinos Center for Biomedical Imaging, Boston, MA, 02129, USA (e-mail: JGEROLD1@mgh.harvard.edu; kchan2@mgh.harvard.edu; YJUN@mgh.harvard.edu; sfujita@mgh.harvard.edu; abhatt7@mgh.harvard.edu; YMA12@mgh.harvard.edu; HLEE84@mgh.harvard.edu; Susie.Huang@mgh.harvard.edu; BBILGIC@mgh.harvard.edu).

B. Bilgic and I. Jelescu share joint last authorship.

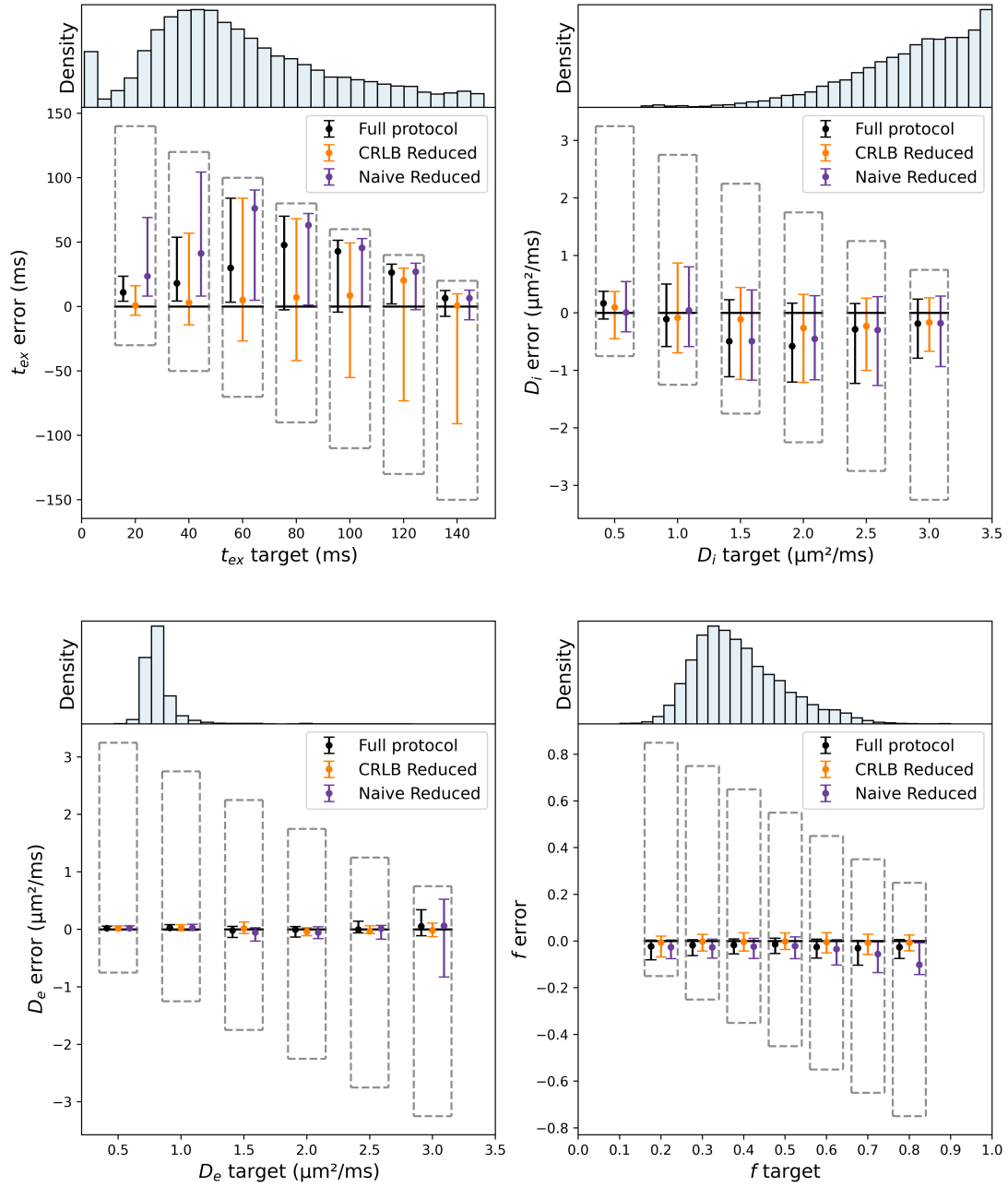


Fig. S1. Estimation errors from synthetic simulations: full protocol vs. FIM and naive subprotocols. Boxplots show absolute errors in parameter estimation (t_{ex} , f , D_i , D_e) for synthetic NEXI signals corrupted with Gaussian noise ($\text{SNR}=32\pm 26$). Dashed boxes represent model fitting bounds. Both reduced subprotocols show increased error and variance compared to the full protocol, particularly for t_{ex} and f , with the naive protocol exhibiting the poorest performance overall. The FIM protocol performs slightly better but still fails to match the accuracy of the XAI-optimized protocol (see main Fig.3).

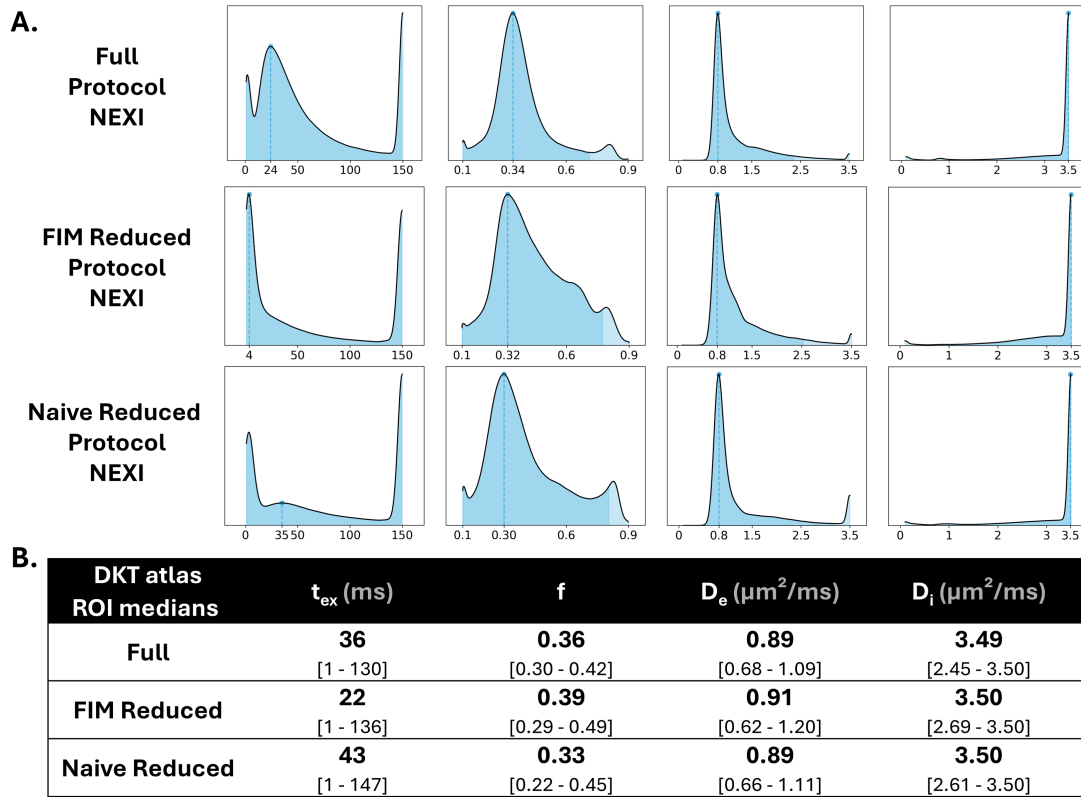


Fig. S2. Distributions and summary of NEXI parameter estimates across DKT cortical regions for full, FIM-reduced, and naïve-reduced protocols. (A) Kernel density estimates of voxel-level values for each NEXI parameter (t_{ex} , f , D_e , D_i), aggregated across all DKT ROIs and all subjects. The full protocol (top row) serves as the reference. The FIM-reduced protocol (middle row) and Naïve-reduced protocol (bottom row) show clear discrepancies compared to the full protocol. For t_{ex} and f , the FIM-reduced protocol exhibits bimodal or flattened distributions, losing the characteristic shape observed in the full protocol. The Naïve-reduced protocol also shows altered distributions, particularly for t_{ex} , with an even stronger ceiling effect and a loss of detail in the lower range. The vertical dashed lines indicate the mode of each distribution. (B) Summary statistics computed from ROI-wise medians across the cortex. Median values and ranges reveal substantial differences between the full protocol and the FIM-reduced and Naïve-reduced protocols, particularly for t_{ex} and f , where the FIM-reduced protocol shows a highly lower median and range for t_{ex} . These results highlight the limitations of FIM-based and heuristic subsampling in preserving accurate parameter estimates and their distributions.

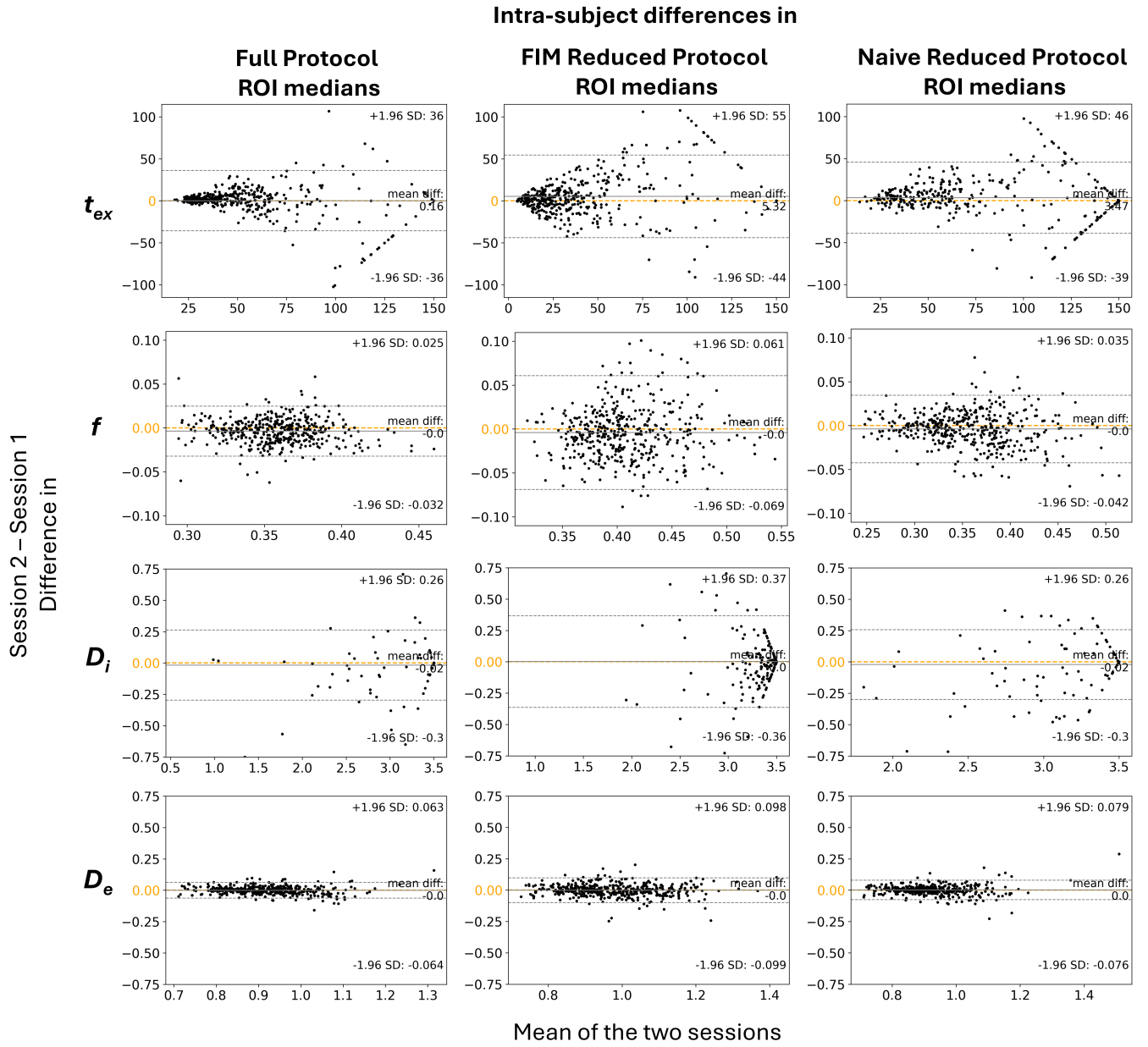


Fig. S3. Test–retest reproducibility of full, FIM-derived, and naive subprotocols. Bland–Altman plots show intra-subject differences in DKT ROI medians between repeated sessions for t_{ex} , f , D_i , and D_e . Compared to the full protocol (left), both the FIM-reduced (center) and naive (right) protocols exhibit increased variability, but the patterns differ across parameters. The FIM protocol shows a marked increase in variability for f and mild dispersion increases for t_{ex} and D_i . In contrast, the naive protocol shows only modest increases in spread for t_{ex} and f , while maintaining similar agreement for D_i and D_e . Compared to the XAI-optimized subprotocol (Fig. 8), which closely matches full protocol reproducibility, both FIM and naive strategies perform worse, especially for f in the FIM case. This confirms that parameter robustness can degrade differently depending on the feature selection strategy and emphasizes the importance of task-aware protocol design for robust parameter estimation in repeat studies.

Supplementary Comparison Across Scanners and Pipelines

To contextualize our current results on the CONNECTOM 2.0 scanner, we compared group-level NEXI parameter estimates to those obtained in our previous studies using both CONNECTOM 1.0 and PRISMA scanners. The CONNECTOM 1.0 dataset comprised data from four healthy adults (Age: 30.5 ± 3.8 years) acquired on a 3T scanner with 300 mT/m gradients. The acquisition protocol used b-values from 1.0 to 7.5 ms/ μm^2 , at four Δ from 20 to 49 ms, with a fixed gradient duration of $\delta=9$ ms. The protocol totaled 700 volumes and 45 minutes of scan time [14]. The PRISMA dataset included data from 11 healthy adults (Age: 26.9 ± 1.3 years) scanned on a 3T system with 80 mT/m gradients. This protocol, requiring a total of 27 minutes, sampled b-values from 1.0 to 5.0 ms/ μm^2 at five Δ from 28.3 to 65.0 ms, with a fixed gradient duration of $\delta=16.5$ ms and 20 directions per shell, totaling 325 volumes [15]. The two supplementary tables below summarize values across cortical regions using either the mode of means (Table S1) or the mean of medians (Table S2), allowing fair comparison across acquisition hardware, denoising strategies, and modeling variants (e.g., standard NEXI vs. SMEX). Notably, t_{ex} is consistently longer and D_i reaches upper bounds more frequently in the CONNECTOM 2.0 data, likely reflecting its higher gradient strength and sensitivity to fast intra-neurite dynamics. At the same time, inter-scanner discrepancies in f and D_e remain modest. These cross-platform results highlight both the potential and challenges of interpreting NEXI parameters across hardware configurations and processing choices.

TABLE S1

SUMMARY OF NEXI PARAMETER ESTIMATES USING THE *mode of the means* ACROSS DKT CORTICAL REGIONS.

	t_{ex} (ms)	D_i ($\mu\text{m}^2/\text{ms}$)	D_e ($\mu\text{m}^2/\text{ms}$)	f
CONNECTOM 2.0 (Complex)	55.7 [6.1 – 116.6]	3.26 [2.35 – 3.50]	1.12 [0.84 – 1.41]	0.37 [0.29 – 0.44]
PRISMA NEXI (Magnitude)	41.1 [15.5 – 66.7]	2.61 [2.03 – 3.20]	1.59 [1.18 – 2.00]	0.51 [0.41 – 0.61]
PRISMA SMEX (Wide Pulses)	36.8 [17.6 – 58.0]	2.45 [1.99 – 2.90]	1.23 [0.88 – 1.61]	0.42 [0.34 – 0.50]

TABLE S2

COMPARISON OF NEXI PARAMETER ESTIMATES USING THE *mean of DKT medians* WITH 95% CONFIDENCE INTERVALS (CI).

	t_{ex} (ms)	D_i ($\mu\text{m}^2/\text{ms}$)	D_e ($\mu\text{m}^2/\text{ms}$)	f
CONNECTOM 1.0 (NEXI _{RM})	42.3 [40.0 – 44.7]	3.35 [3.32 – 3.38]	0.92 [0.91 – 0.93]	0.38 [0.379 – 0.389]
CONNECTOM 2.0 (Complex)	57.9 [23.2 – 150.0]	3.40 [2.26 – 3.50]	0.92 [0.75 – 1.12]	0.36 [0.30 – 0.41]

Impact of denoising strategy on signal modeling and parameter estimation

Although complex-valued denoising is often favored in diffusion MRI for its minimal bias under Gaussian noise assumptions, its superiority for model fitting is not guaranteed in practice. In this section, we compare model–data agreement and parameter estimates between two processing pipelines: (i) complex-valued MP-PCA denoising with standard NEXI fitting, and (ii) magnitude denoising with Rician mean correction (NEXI_{RM}). Figure S4 evaluates model fit quality against mean cortical signals. This result emphasize the importance of empirically validating denoising choices, especially under conditions of high diffusion weighting or limited SNR, rather than relying solely on theoretical bias arguments.

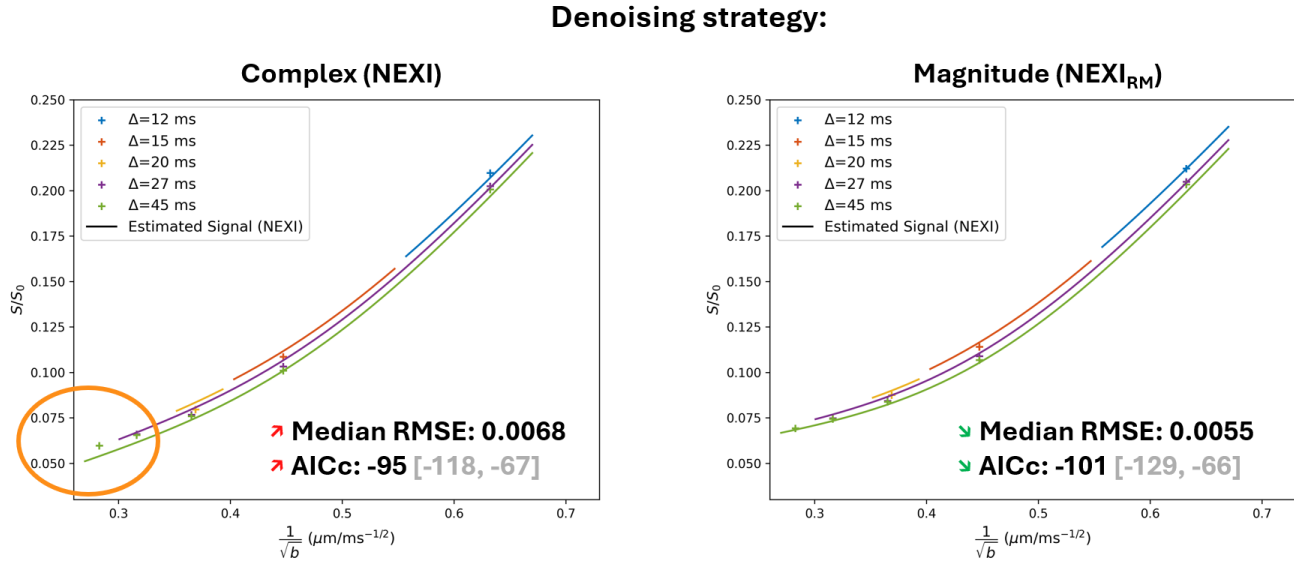


Fig. S4. Comparison of NEXI model fitting using complex vs. magnitude-denoised data. Mean cortical diffusion signals are plotted as a function of $1/\sqrt{b}$ for each diffusion time Δ (color-coded), along with the corresponding NEXI model fit (black lines). Left: Complex-valued MP-PCA denoising followed by standard NEXI fitting. Right: Magnitude-based denoising followed by Rician-mean corrected NEXI fitting (NEXI_{RM}). Although complex denoising is theoretically less biased, it yields a higher residual median RMSE (0.0068) and worse AICc (−95) compared to the magnitude-based pipeline (RMSE = 0.0055, AICc = −101). Notably, a visible mismatch appears for high b -values (i.e., low $1/\sqrt{b}$) and long diffusion times ($\Delta = 45$ ms, green) in the complex case, suggesting a deviation between signal and model fit that is not present in the magnitude-based pipeline. This difference may reflect a residual model inadequacy at high diffusion weighting or subtle SNR-driven effects. These results underscore the need to empirically evaluate model–data agreement even under theoretically optimal denoising conditions.

Extension to High-Resolution Acquisition

To assess our protocol's performance in a high-resolution setting and address the challenge of partial volume effects (PVE), an exploratory acquisition was performed on one subject using the reduced 8-feature protocol at 1.6 mm isotropic resolution. To compensate for the lower Signal-to-Noise Ratio (SNR) at this finer resolution, the total number of diffusion directions was increased to 1,000 across all shells (including $3 \times b = 0$, 80 directions each at $b = 1000$ and $b = 2500$, 128 at $b = 5000$, 136 at $b = 7350$, and 256 at $b = 12500$ for each Δ). Consequently, the repetition time was extended to $TR = 4100$ ms and the matrix size to 138×138 with 82 axial slices. This resulted in a 69-minute scan, during which the mean SNR decreased only moderately, from 32 (CI: [13, 60]) at 2 mm to 27 (CI: [11, 56]) at 1.6 mm. The resulting NEXI parameter maps remained qualitatively consistent with those obtained at 2 mm resolution, as shown both on the cortical surface (Fig. S5) and in axial slices (Fig. S6). High-resolution acquisitions provided sharper delineation of the cortical ribbon and improved contrast at the gray-white matter boundary, particularly for f and D_i , with no indication of increased instability in model fitting. These results demonstrate that our reduced protocol can be leveraged for more accurate and reliable cortical mapping when extended scan durations are feasible.

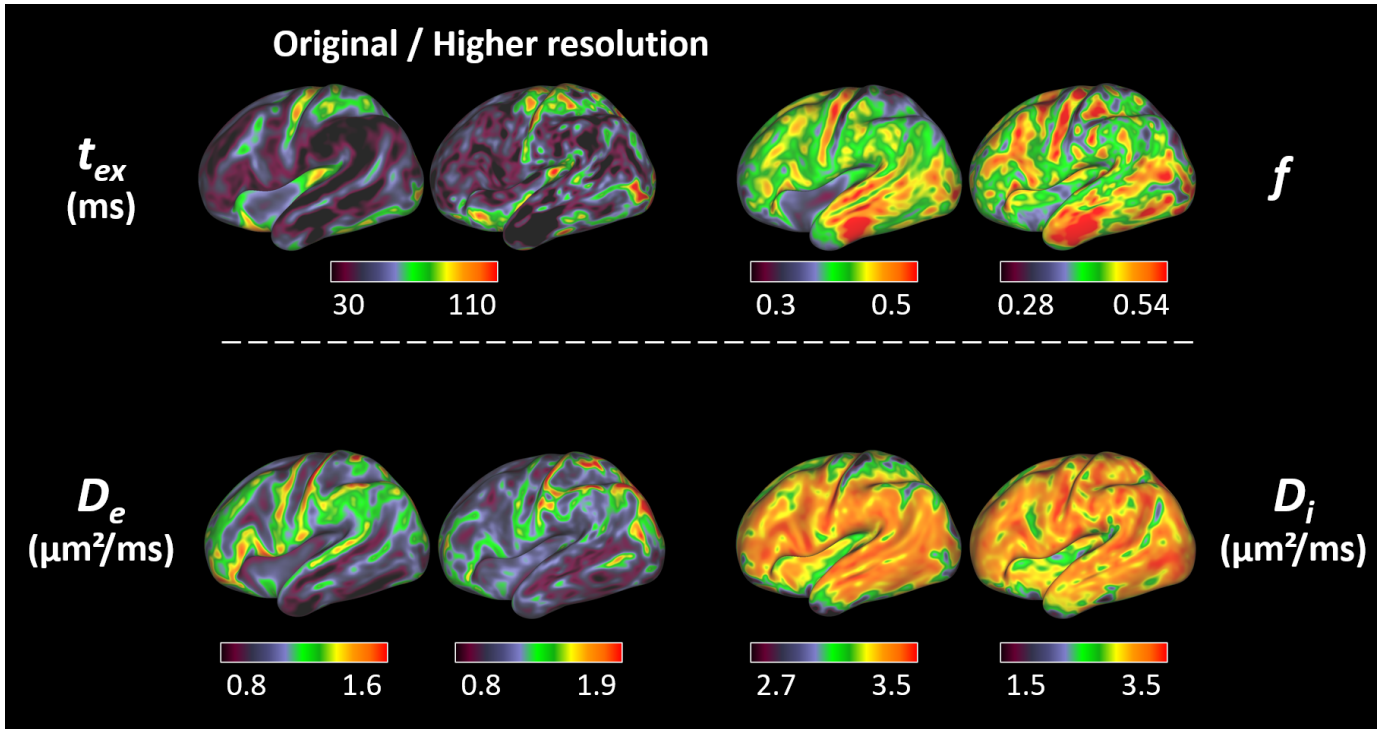


Fig. S5. Surface-based comparison of NEXI parameters at standard (2.0 mm) and high (1.6 mm) resolution. Spatial distributions are largely preserved across resolutions, confirming the robustness of parameter estimation under increased spatial detail. Notably, subtle differences emerge in fine anatomical structures, particularly in f and t_{ex} , suggesting improved delineation of regional heterogeneity at higher resolution. Slight increases in parameter range (as seen in colorbars) may reflect reduced partial volume effects and enhanced anatomical specificity. This confirms that the reduced 8-feature protocol remains robust at higher spatial resolution and may support laminar or fine-grained microstructural analyses in longer acquisitions.

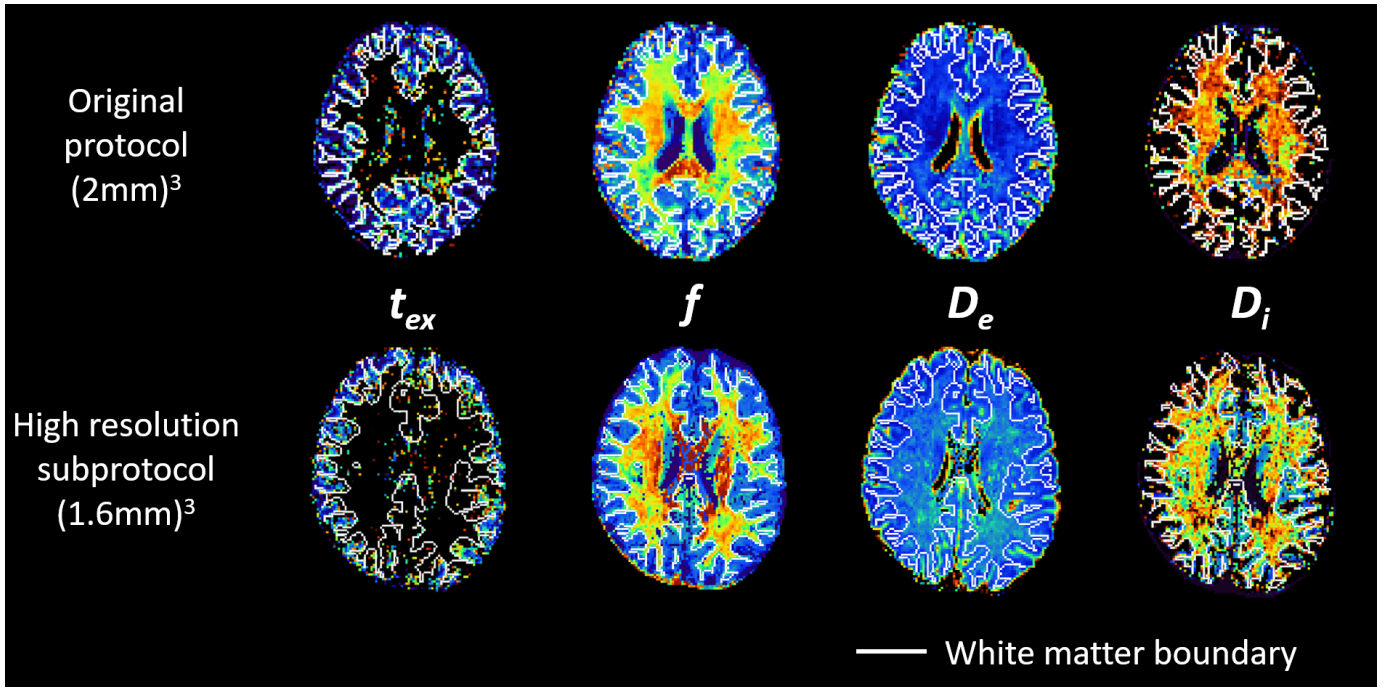


Fig. S6. Axial slice comparison of NEXI parameter maps at standard (2.0 mm) and high (1.6 mm) isotropic resolution. Maps of t_{ex} , f , D_e , and D_i are displayed across the same mid-cortical axial slice in a single subject, comparing the original full protocol (top row) to the high-resolution version of the reduced 8-feature protocol (bottom row). Despite the smaller voxel size, parameter estimates remain qualitatively consistent, confirming the protocol's robustness across spatial resolutions. High-resolution maps reveal sharper gray-white matter boundaries (highlighted in white), improved delineation of cortical ribbon structure, and increased local contrast, especially for f and D_i . These enhancements suggest that the reduced protocol supports fine-grained anatomical mapping, and may be suitable for studies targeting laminar profiles or subtle cortical microstructural changes.

While the 69-minute scan duration was substantial, it was a direct consequence of the physical trade-off required to maintain image quality at finer spatial scales. The voxel volume was reduced by a factor of approximately 2, necessitating a four-fold increase in diffusion measurements to compensate for the inherent drop in SNR. This compensated acquisition represents the optimal NEXI protocol for this high resolution; a full 15-feature protocol would have been prohibitively long at nearly 140 minutes. The robustness of the parameter maps at this scale holds promise for future applications aimed at mitigating partial volume effects.